RSC Advances

PAPER

View Article Online
View Journal | View Issue

Cite this: *RSC Adv.*, 2026, **16**, 9858

Theoretical insights into the stability and nature of nonconventional C–H···Y (Y=N, P, As, Sb) hydrogen bonds in haloform–pnictogen trihydride complexes

Khanh Ngoc Pham,[a] Dang Thi Anh Thu,[b] Bui Duc Ai[b] and Nguyen Tien Trung *[bc]

In this study, we investigate the stability and intrinsic nature of nonconventional C–H···Y hydrogen bonds (Y=N, P, As, Sb), with special attention given to the largely unexplored C–H···P interaction and the first theoretical observation of C–H···As/Sb interactions in complexes formed between haloforms (CHX_3, X = F, Cl, Br) and pnictogen trihydrides (YH_3, Y=N, P, As, Sb). The hydrogen-bond strength in the considered complexes increases in the order C–H···Sb < C–H···As ≈ C–H···P < C–H···N, with C–H···N being about two to three times stronger than C–H···Sb. The C–H stretching frequency shifts in the formed hydrogen bonds are predominantly red-shifting, increasing in the order C–H···As ≈ C–H···P < C–H···Sb < C–H···N. The larger red shifts observed for the C–H···Sb hydrogen bonds relative to the corresponding C–H···P/As ones arise from the high polarizability of the proton acceptor and the associated increase in the σ^*(C–H) antibonding orbital population, whereas in the C–H···N hydrogen bonds the enhancement of the C–H stretching frequency red shift from X = F to Cl to Br is primarily driven by stronger electrostatic interactions between the interacting atoms. Symmetry-Adapted Perturbation Theory (SAPT) analyses reveal that the C–H···N hydrogen bonds are predominantly electrostatic in nature, whereas the C–H···P/As/Sb interactions exhibit a more balanced interplay of attractive contributions, with dispersion becoming increasingly important for heavier halogens and pnictogens. By extending the analysis as a function of the C···Y distance, we find that the C–H···N hydrogen bonds remain red-shifting and dominated by electrostatic interactions over the entire distance range, while the C–H···P/As/Sb interactions exhibit induction-driven blue shifts at short separations and dispersion-dominated red shifts at larger distances.

Received 10th January 2026
Accepted 13th February 2026

DOI: 10.1039/d6ra00247a

rsc.li/rsc-advances

1. Introduction

Hydrogen bonding is one of the most fundamental noncovalent interactions governing molecular structure and reactivity in chemistry, biology, and materials science.[1,2] In biological systems, it supports essential functions such as the stabilization of protein secondary structures,[3,4] the specificity of DNA base-pairing,[5,6] and the maintenance of the collagen triple helix.[7] Beyond its biological roles, hydrogen-bonding motifs have been widely exploited in materials design, including improving the performance of polymer semiconductors,[8,9] enabling dynamic self-healing networks in elastomers and supramolecular liquid-crystal polymers,[10–12] and supporting the development of hydrogen-bond-cross-linked polymers for biomedical applications.[13,14] Hydrogen bonding further plays a decisive role in stabilizing chain conformations in cellulose and related saccharides.[15,16] Recent studies have shown that condensed-phase environments, particularly ionic liquids, can strongly modulate hydrogen-bond energetics through cooperative interactions involving multiple hydrogen-bonding sites, highlighting the importance of solvent structure in shaping hydrogen-bond behavior beyond the gas phase.[17,18] Therefore, a deep understanding of its fundamental nature is essential for elucidating molecular behavior in chemical and biological systems and for guiding the rational development of advanced functional materials.

In general, an A–H···B hydrogen bond involves interaction between an electron-deficient hydrogen atom and an electron-rich atom or group, such as F, N, O, or a π-system. This interaction is primarily electrostatic in nature,[19,20] but hyperconjugation n(B) → σ^*(A–H) and partial covalent interactions can also contribute.[21–24] Formation of such a hydrogen bond typically weakens the donor A–H bond, leading to its elongation and a decrease in its vibrational stretching frequency relative to

[a]*Faculty of Food Science and Technology, Ho Chi Minh City University of Industry and Trade (HUIT), 140 Le Trong Tan street, Ho Chi Minh City, Vietnam*
[b]*Laboratory of Computational Chemistry and Modelling (LCCM), Quy Nhon University, 170 An Duong Vuong Street, Quy Nhon Nam 590000, Vietnam*
[c]*Faculty of Natural Sciences, Quy Nhon University, 170 An Duong Vuong Street, Quy Nhon Nam 590000, Vietnam. E-mail: nguyentientrung@qnu.edu.vn*

the isolated A–H monomer, which is referred to as a red shift. However, many studies have shown that some A–H···B hydrogen bonds shorten the A–H bond and shift its stretching frequency to higher values, forming blue-shifting hydrogen bonds.[25–27] Numerous theoretical models have been advanced to account for the origin of blue-shifting hydrogen bonds,[28–39] but each captures only part of the underlying physical picture. To gain a deeper understanding of hydrogen-bonding behavior, several researchers extended their analyses beyond equilibrium structures and examined these interactions along the potential energy surface, often in combination with energy-decomposition analyses. Using fluoroform complexes as an example, some studies described the blue shift as a long-range effect driven by electrostatic interactions.[25,29] In contrast, Mao and Head–Gordon argued that the blue shift was fundamentally a short-range phenomenon.[35] More recently, Huynh *et al.* demonstrated that blue-shifting is governed by short-range interactions, while red-shifting behavior is dominated by long-range forces.[40] These differing observations highlight the need for further systematic investigations to achieve a unified understanding of this behavior of hydrogen bond, and addressing this issue forms an important part of the present work.

Over the past decade, C–H···N hydrogen bonds have been extensively studied in a wide range of molecular systems and under various conditions with both blue- and red-shifting behaviors reported. Blue shifts have been frequently observed in various haloform complexes,[41–49] whereas red shifts are found in systems involving haloforms interacting with NH_3, PH_3, CH_3OH, H_2O.[41,46,50] The direction of the shift depends strongly on the specific donor–acceptor pair. For instance, studies of haloform–NH_3 and haloform–monohalogenated amine complexes show that their C–H···N stretching shifts vary systematically with the polarity of the C–H bond and the proton affinity of the nitrogen site.[31] Still, despite these extensive studies, a comprehensive understanding of all factors governing C–H···N shifting behavior remains incomplete.

Furthermore, beyond the proton–acceptor atom in the first row of the Group-15 congeners (*i.e.*, nitrogen), it is important to extend systematic investigations to the heavier members of the group, including phosphorus (P), arsenic (As), and antimony (Sb). Phosphorus is indispensable for all forms of life and is a key component of biomolecules, including adenosine triphosphate,[51] whereas arsenic and antimony, despite their well-known toxicity, play important roles in geochemistry and environmental processes.[52,53] These heavier elements also differ significantly from nitrogen in polarizability, electronic structure, and bonding behavior, making the study of their hydrogen-bond interactions valuable for expanding our understanding of nonconventional hydrogen bonding. Hansen *et al.* demonstrated that phosphorus can function as a genuine hydrogen-bond acceptor in O–H···P interactions, with an acceptor strength comparable to that of oxygen and sulfur, though generally weaker than nitrogen.[54] Baburao *et al.* investigated the nature and strength of C–H···P hydrogen bonds, but a detailed understanding of the individual energetic contributions governing these interactions is still lacking.[46] It is noteworthy that analogous hydrogen bonds involving As or Sb have not been reported, although halogen bonds to these heavier elements have been studied in the solid state.[55] This underscores the need for a systematic comparison of these interactions with the well-studied C–H···N hydrogen bond.

Motivated by the challenges outlined above, we investigate the interactions between CHX_3 (X = F, Cl, Br) and YH_3 (Y=N, P, As, Sb) to elucidate the intrinsic nature and systematic trends of C–H···N/P/As/Sb hydrogen bonds. In the first part of this work, atoms-in-molecules (AIM) and natural bond orbital (NBO) analyses are employed to characterize and compare the nature and strength of the hydrogen bonds formed in these complexes, with particular attention to the underexplored C–H···As/Sb interactions. High-order symmetry-adapted perturbation theory (SAPT) is then used to dissect the individual energy components that govern the observed shifts in the C–H stretching frequencies. We also examine how variations in the halogen atom (X) and the Group-15 central atom (Y) influence the strength and characteristics of these hydrogen bonds. In the second part, we focus on $CHCl_3$···YH_3 complexes due to medium polarity of C–H in $CHCl_3$ as compared to CHF_3 and $CHBr_3$ isolated monomers and investigate the C–H···N/P/As/Sb hydrogen bonds as a function of intermolecular separation along the potential energy surface, in order to gain deeper insight into the origin and evolution of their blue- and red-shifting vibrational behavior.

2. Computational methods

All quantum-mechanical calculations were performed using the Gaussian 16 software package.[56] Geometry optimizations for all complexes and the corresponding isolated monomers were carried out at second-order Møller–Plesset perturbation (MP2) theory level with the aug-cc-pVTZ basis set, except for Sb-containing systems, for which the aug-cc-pVTZ-PP basis set was used. Harmonic vibrational frequency calculations were performed at the same MP2 level with the same basis sets to confirm that the optimized structures correspond to true minima on the potential-energy surface and to obtain the associated zero-point vibrational energies (ZPEs), which were evaluated according to

$$E_{\mathrm{ZPE}} = \sum_{i}^{3N-5/6} \frac{1}{2} h\nu_i \tag{1}$$

where ν_i denotes the i-th vibrational frequency and N is the number of atoms in the system.

Single-point electronic energies for all complexes and monomers were calculated at the coupled-cluster with singles, doubles, and perturbative triples [CCSD(T)] level using the aug-cc-pVTZ basis set, except for systems containing Sb atoms, for which the aug-cc-pVTZ-PP basis set was employed. The interaction (int) energy of each complex was then evaluated as follows:

$$\Delta E^{*}_{\mathrm{int}} = \left(E^{\mathrm{CCSD(T)}} + E^{\mathrm{MP2}}_{\mathrm{ZPE}}\right)\mathrm{complex} - \left(E^{\mathrm{CCSD(T)}} + E^{\mathrm{MP2}}_{\mathrm{ZPE}}\right)\mathrm{monomer} + E^{\mathrm{CCSD(T)}}_{\mathrm{BSSE}} \tag{2}$$

Here, BSSE is the basis set superposition error computed at the same level of theory and with the same basis sets as the single-point energies using the counterpoise method of Boys and Bernardi.[57]

To further elucidate the origin and variability of the hydrogen-bond strengths, we also evaluated the deprotonation enthalpies (DPE) of the C–H bonds and the proton affinities (PA) of the Y atom in the corresponding YH_3 monomers. These quantities were computed at the same level of theory as the interaction energies to ensure internal consistency.

The AIMAll program[58] based on the Quantum Theory of Atoms in Molecules (QTAIM)[59–61] was employed to compute the topological parameters of the complexes using wavefunctions obtained at the MP2/aug-cc-pVTZ level, except for Sb-containing systems, for which the MP2/aug-cc-pVTZ-PP level was employed. In this analysis, the presence of bond critical points (BCPs), which signify the existence of hydrogen bonds, was identified. Then at each BCP, we calculated the electron density [$\rho(r)$], the Laplacian of the electron density [$\nabla^2\rho(r)$], and the electron energy density [$H(r)$], which is the sum of the potential energy density [$V(r)$] and the kinetic energy density [$G(r)$], to further characterize the hydrogen bonds. The individual hydrogen-bond energies (E_{HB}) were estimated using the Espinosa–Molins–Lecomte formula.[62] In addition, non-covalent interaction (NCI) analysis, performed at the same computational level as the QTAIM calculations, was used to visually examine and confirm the weak intermolecular interactions present in the complexes.[63,64]

To probe electron transfer and further elucidate the nature of the nonconventional hydrogen bonds, Natural Bond Orbital (NBO)[65] analysis was carried out using the NBO 7.0 program at the same level of theory as the AIM analysis. Symmetry-adapted Perturbation Theory (SAPT2+) with the def2-TZVPD basis set, calculated using the PSI4 software package,[66] were employed to quantitatively analyze the contributions of individual energy components to the stability of the complexes and to provide intrinsic insight into the characteristics of the hydrogen bonds. Within the SAPT framework, the total interaction energy is decomposed into four primary terms: electrostatic (E_{elst}), induction (E_{ind}), exchange (or Pauli repulsion, E_{exch}), and dispersion energy (E_{disp}), along with δE_{HF} which includes the third and higher-order induction and exchange-induction terms.

3. Results and discussion

3.1. Formation and strength of hydrogen bonds in studied complexes

In our search for stable structures of the $CHX_3\cdots YH_3$ complexes, we found that the anisotropic electrostatic potential of CHX_3 (X = F, Cl, Br), arising from its polar C–X bonds and carbon-centered σ-hole, together with the directional lone pair of YH_3 (Y=N, P, As, Sb), can lead to form a single C–H···Y hydrogen-bonding motif. However, because both CHX_3 and YH_3 possess C_{3v} symmetry, rotation around the C–H···Y axis allows this same interaction to adopt two distinct and energetically stable orientations. These correspond to 12 complexes with a staggered geometry (**XY-1**), where the Y–H bonds lie between the three X atoms, and 12 complexes with an eclipsed geometry (**XY-2**), where they align directly with the C–X bonds. These two configurations belonging to C_{3v} point group are characterized by the X–C···Y–H dihedral angle, which is 60° in **XY-1** geometry and 0° in **XY-2** one. The stable geometries of all complexes with their intermolecular distances are shown in Fig. S1a and S1b in the (SI), and one representative example is illustrated in Fig. 1.

The formation and strength of C–H···Y hydrogen bonds in the investigated complexes can be first assessed by analyses of intermolecular distances together with AIM and NCI results. As shown in Table 1, the optimized H···Y distances in the complexes are generally shorter than, or comparable to, the sums of the van der Waals radii of the interacting atoms. Specifically, the H···N, H···P, H···As, and H···Sb distances fall within 2.08–2.30 Å, 2.62–2.94 Å, 2.64–2.92 Å, and 2.76–3.14 Å, respectively, compared with van der Waals radii sums of 2.65 Å, 2.90 Å, 2.95 Å, and 3.16 Å. These geometric features provide initial evidence for the presence of weak C–H···Y interactions. Theoretical results reported that existence of weak nonconventional C–H···Y hydrogen bonds is typically associated with relatively long H···Y distances, often on the order of ~2.5–3.5 Å, which depends on both proton donor and acceptor.[2,21] Further evidence is provided by BCPs identified in the AIM analysis (Fig. S2), whose electron densities ($\rho(r)$) (0.008–0.025 au) and Laplacians ($\nabla^2(\rho(r))$) (0.020–0.068 au) fall within the typical range of weak interaction formation.[67] Additional support comes from NCI analysis in Fig. S3, which shows the negative sign(λ_2) $\rho(r)$ peaks with the reduced gradient (RDG) values of 0.01–0.03 au, affirming the presence of the C–H···Y hydrogen bonds in the considered complexes.[64] This observation is also consistent with our earlier findings in the different complexes.[68–71]

The hydrogen-bond energies associated with the two geometric forms, the eclipsed and staggered conformations, show almost no difference, with the largest deviation being only 0.4 kJ mol^{-1} between the **FBr-1** and **FBr-2** complexes (see Table 1). For complexes that share the same CHX_3 proton donor, the strength of the C–H···Y hydrogen bonds in the complexes increases in the order C–H···Sb < C–H···As ≈ C–H···P < C–H···N. Specifically, the hydrogen-bond energies (E_{HB}) rise from −8.0 to −4.3 kJ mol^{-1} for C–H···Sb, −10.7 to −5.5 kJ mol^{-1} for C–H···As and −10.3 to −4.8 kJ mol^{-1} for C–H···P, reaching −23.4 to −12.3 kJ mol^{-1} for the strongest C–H···N interactions (Table 1). This corresponds to an approximately two-to three-fold increase in interaction strength when Y goes from Sb to N, highlighting a clear and systematic enhancement across the series. We observe that the C–H···N hydrogen bonds in $CHX_3\cdots NH_3$ (X = F, Cl) complexes are slightly stronger than those reported previously at the MP2/6-311++G(d,p) level.[36] However, for $CHBr_3\cdots NH_3$ the difference reaches up to 3 kJ mol^{-1}, underscoring the importance of using high level of theory when heavy atom such as Br is involved.

The observed enhancement in the strength of the C–H···Y hydrogen bonds correlates with the increasing electron densities $\rho(r)$ at the BCPs as Y changes from Sb to As to P and finally to N. Notably, the BCP electron densities associated with C–H···

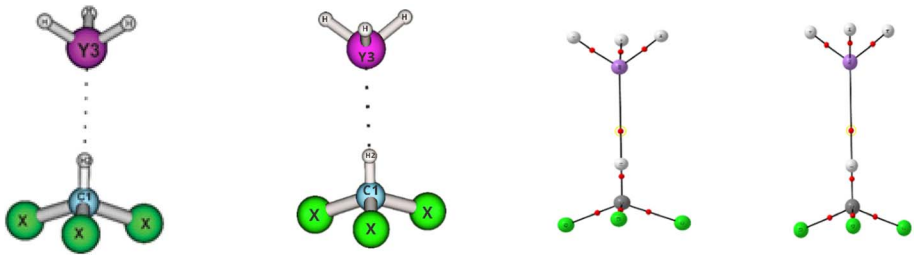

Fig. 1 Stable structure and topological feature of the complexes with staggered (XY-1) and eclipsed geometries (XY-2) (X = F, Cl, Br and Y=N, P, As, Sb).

N/P interactions in $CHX_3\cdots YH_3$ (X = F, Cl and Y=N, P) agree within 0.01 au with those obtained at the B3LYP/6-311++G(d,p) level, whereas deviations of up to 0.1 au are observed for $CHBr_3\cdots PH_3$.[46] This again emphasizes the need for high-level theoretical methods for Br-containing systems. The systematic increase in the C–H···Y hydrogen-bond strength when Y varies from Sb to N is further supported by the progressively more negative NBO charges on Y (Table 2), increasing its electron-accepting ability and strengthening the electrostatic component of the H···Y interaction. Additional evidence comes from the proton affinities of the YH_3 monomers, rising in the order $SbH_3 < AsH_3 < PH_3 < NH_3$, with computed values of 752, 766, 783, and 847 kJ mol^{-1}, respectively, obtained at the CCSD(T)/aug-cc-pVTZ level, except for Sb-containing systems, for which the aug-cc-pVTZ-PP basis set was used. We note that the good agreement between these calculated PA values and their experimental values[72] confirms the reliability of the computational method used. Finally, the superior strength of the C–H···N interaction is evident from the much smaller $r_{H\cdots Y}/\sum r_{vdW}$ ratios for C–H···N (0.78–0.87) relative to C–H···P/As/Sb (0.87–1.05), as shown in Table 1.

For complexes containing the same YH_3 proton acceptor, the C–H···Y hydrogen bond becomes progressively stronger as X in CHX_3 changes from F to Cl to Br. This ordering is consistent with the results reported by Man *et al.* for $CHX_3\cdots NH_2Y$ complexes (X = F, Cl, Br; Y=H, F, Cl, Br).[36] In line with the analysis for fixed proton acceptors above, this trend is supported by the more negative hydrogen-bond energies, smaller $r_{H\cdots Y}/\sum r_{vdW}$ ratios, and decreasing deprotonation enthalpies observed from CHF_3 to $CHCl_3$ to $CHBr_3$, with values of 1586, 1506, and 1483 kJ mol^{-1}, respectively. We also note that the calculated DPE values closely match those reported in previous studies.[36,73]

The formation and strength of the hydrogen bonds are also examined by the NBO analysis. As shown in Table 2, the total electron-density transfer (EDT) of CHX_3 in all complexes is

Table 1 The topological parameters of the nonconventional C–H···Y (Y=N, P, As, Sb) hydrogen bonds in the stable complexes

Complex	Nonconventional hydrogen bond	$r_{H\cdots Y}$ (Å)	$\rho(r)$ (au)	$\nabla^2\rho(r)$ (au)	$H(r)$ (au)	E_{HB} (kJ mol^{-1})	$r_{H\cdots Y}/\sum r_{vdW}$
FN-1	C1–H2···N3	2.30	0.016	0.048	0.013	−12.3	0.87
FP-1	C1–H2···P3	2.94	0.008	0.020	0.0007	−4.8	1.03
FAs-1	C1–H2···As3	2.92	0.009	0.021	0.0006	−5.5	1.05
FSb-1	C1–H2···Sb3	3.12	0.008	0.017	0.0004	−4.3	1.02
ClN-1	C1–H2···N3	2.14	0.022	0.062	0.0003	−19.6	0.81
ClP-1	C1–H2···P3	2.71	0.013	0.029	0.0003	−8.5	0.93
ClAs-1	C1–H2···As3	2.72	0.014	0.028	0.0001	−8.9	0.92
ClSb-1	C1–H2···Sb3	2.85	0.013	0.025	0.0000	−8.0	0.90
BrN-1	C5–H6···N3	2.08	0.025	0.068	−0.0003	−23.0	0.78
BrP-1	C1–H2···P3	2.62	0.015	0.033	0.0001	−10.4	0.90
BrAs-1	C1–H2···As3	2.64	0.016	0.032	−0.0001	−10.7	0.89
BrSb-1	C1–H2···Sb3	2.76	0.015	0.028	−0.0003	−9.8	0.87
FN-2	C1–H2···N3	2.30	0.016	0.048	0.0013	−12.3	0.87
FP-2	C1–H2···P3	2.94	0.008	0.020	0.0007	−4.8	1.03
FAs-2	C1–H2···As3	2.93	0.009	0.021	0.0006	−5.5	1.05
FSb-2	C1–H2···Sb3	3.14	0.008	0.017	0.0004	−4.3	1.02
ClN-2	C1–H2···N3	2.14	0.022	0.062	0.0003	−19.6	0.81
ClP-2	C1–H2···P3	2.71	0.013	0.029	0.0004	−8.4	0.93
ClAs-2	C1–H2···As3	2.72	0.014	0.028	0.0002	−8.9	0.92
ClSb-2	C1–H2···Sb3	2.85	0.013	0.026	0.0000	−8.0	0.90
BrN-2	C1–H2···N3	2.08	0.025	0.068	−0.0004	−23.4	0.78
BrP-2	C1–H2···P3	2.63	0.015	0.032	0.0001	−10.3	0.91
BrAs-2	C1–H2···As3	2.64	0.016	0.032	−0.0001	−10.7	0.89
BrSb-2	C1–H2···Sb3	2.77	0.015	0.028	−0.0002	−9.7	0.88

Table 2 NBO analysis of the stable complexes

Complex	Nonconventional hydrogen bond	EDT[a] (e)	E_{inter}[b] (kJ mol^{-1})	ΔE_{intra}[c] (kJ mol^{-1})	q(H2) (e)	q(Y3) (e)	$\Delta\sigma^*$ (C1–H2)[d] (10^{-3} e)	Δs% (C1)[e] (%)[e]
FN-1	C1–H2···N3	0.01	33.0	−17.3	0.155	−1.079	1.0	2.2
FP-1	C1–H2···P3	0.01	17.4	−8.2	0.129	0.016	2.0	1.3
FAs-1	C1–H2···As3	0.01	20.2	−8.4	0.128	0.087	3.3	1.3
FSb-1	C1–H2···Sb3	0.01	24.2	−3.5	0.118	0.363	5.8	0.5
ClN-1	C1–H2···N3	0.02	37.5	−22.7	0.264	−1.075	3.5	3.0
ClP-1	C1–H2···P3	0.01	22.2	−14.1	0.236	−0.004	4.7	1.7
ClAs-1	C1–H2···As3	0.02	23.9	−7.5	0.234	0.086	6.5	1.8
ClSb-1	C1–H2···Sb3	0.02	24.0	−7.3	0.229	0.367	8.9	1.6
BrN-1	C1–H2···N3	0.03	40.0	−22.3	0.263	−1.075	5.0	3.8
BrP-1	C1–H2···P3	0.02	26.3	−9.4	0.236	−0.002	6.1	2.4
BrAs-1	C1–H2···As3	0.02	27.2	−9.2	0.233	0.088	8.0	2.4
BrSb-1	C1–H2···Sb3	0.02	27.3	−8.5	0.228	0.370	10.8	2.3
FN-2	C1–H2···N3	0.01	33.0	−17.3	0.155	−1.079	1.0	2.2
FP-2	C1–H2···P3	0.01	17.3	−8.2	0.129	0.016	2.0	1.3
FAs-2	C1–H2···As3	0.01	20.1	−8.2	0.128	0.087	3.3	1.3
FSb-2	C1–H2···Sb3	0.01	14.0	−3.5	0.118	0.363	5.7	0.5
ClN-2	C1–H2···N3	0.02	37.6	−22.6	0.264	−1.076	3.4	3.0
ClP-2	C1–H2···P3	0.01	22.0	−13.9	0.236	−0.004	4.6	1.7
ClAs-2	C1–H2···As3	0.02	23.9	−14.3	0.234	0.086	6.5	1.7
ClSb-2	C1–H2···Sb3	0.02	23.9	−7.3	0.229	0.367	8.9	1.6
BrN-2	C1–H2···N3	0.03	40.7	−22.3	0.263	−1.075	5.2	3.8
BrP-2	C1–H2···P3	0.02	26.1	−9.2	0.236	−0.002	6.0	2.4
BrAs-2	C1–H2···As3	0.02	27.2	−9.2	0.233	0.088	8.0	2.4
BrSb-2	C1–H2···Sb3	0.02	27.0	−8.4	0.228	0.370	10.6	2.3

[a] Electron density transfer from YH_3 to CHX_3. [b] Intermolecular hyperconjugative energy of electron transfer from n(Y3) to σ^*(C1–H2) orbital. [c] Change of intramolecular hyperconjugation energy of electron transfer from n(Y3) to σ^*(C1–H2) orbital. [d] Change in electron density in σ^*(C1–H2) antibonding orbital. [e] Change in percentage of s-character in C1 hybrid orbital.

negative, demonstrating that electron density is transferred from YH_3 to CHX_3 upon complexation. This direction of charge flow is consistent with the intermolecular electron-transfer energies (E_{inter}) associated with the n(Y3) → σ^*(C1–H2) donation, which range from about 14.0 to 40.7 kJ mol^{-1} for the considered complexes. For complexes with the same proton donor CHX_3, the n(Y3) → σ^*(C1–H2) magnitude is significantly larger for Y=N than for Y=P, As, and Sb. However, this trend does not correlate directly with the hydrogen-bond strength discussed in the AIM analysis. For example, E_{inter} values for the $CHBr_3\cdots YH_3$ complexes decrease from about 40.0 kJ mol^{-1} for Y=N to 27 kJ mol^{-1} for Y=As and Sb and to 26 kJ mol^{-1} for Y=P. However, the larger E_{inter} values for Y=As and Sb relative to Y=P can be attributed to their higher polarizability, which facilitates enhanced electron-density redistribution upon complexation, leading to larger σ^*(C1–H2) populations and stronger polarization-assisted n(Y3) → σ^*(C1–H2) donation. Indeed, the atomic polarizability increases markedly from N ($\alpha = 7.4 \pm 0.2$ au) to P (25.8 ± 1.0 au), As (30 ± 1 au), and Sb (43 ± 2 au).[74] For the complexes containing the same YH_3, the n(Y3) → σ^*(C1–H2) transfer increases systematically as X in CHX_3 changes from F to Cl to Br (Table 2). The larger charge-transfer energies observed for the heavier halogens reflect their stronger electron-donor ability, providing a clear electronic origin for the enhanced C–H···Y hydrogen-bond strength in the $CHBr_3$ and $CHCl_3$ complexes compared with CHF_3.

3.2. Nature of hydrogen bonds in studied complexes

To gain insight into the characteristics of the C–H···Y hydrogen bonds upon complexation, the changes in the C–H bond lengths (Δr, mÅ) and the corresponding shifts in their stretching frequencies ($\Delta\nu$, cm^{-1}) were calculated and are summarized in Table 3. The positive $\Delta r_{(C-H)}$ values, ranging from 0.2 to 7.1 mÅ, together with the negative $\Delta\nu_{(C-H)}$ shifts of approximately −0.3 to −110 cm^{-1}, indicate the formation of red-shifting C–H···Y hydrogen bonds in these complexes. The only exceptions are interactions in the **FP-1** and **FP-2** complexes, which exhibit negligible changes in C–H bond length and nearly zero frequency shifts, indicating that these two hydrogen bonds can be regarded as essentially non-shifting. These negligible changes are in line with earlier study, where $\Delta r_{(C-H)}$ and $\Delta\nu_{(C-H)}$ were only 0.08 mÅ and −2.83 cm^{-1}, respectively, at the B3LYP/6-311++G(d,p) level.[46] As be seen in Table 2, following complexation, the electron density in all σ^*(C–H) orbitals is significantly enhanced in the range of 1.0 to 10.8 me. This enhancement arises from a pronounced intermolecular hyperconjugative charge transfer from the n(Y) lone pair to the σ^*(C–H) antibonding orbital, $E_{inter}[n(Y3) \rightarrow \sigma^*(C1–H2)]$, which is substantially larger than the decreasing magnitude of corresponding intramolecular hyperconjugation energy, $\Delta E_{intra}[n(Y3) \rightarrow \sigma^*(C1–H2)]$ (Table 2). In addition, a modest increase of 0.5–3.8% in the s-character of the C1(H2) orbital is also observed for all complexes. Thus, the observed red shift of the C–H

Table 3 Changes in the C1–H2 bond length (Δr, mÅ) and stretching frequency ($\Delta\nu$, cm^{-1}) upon hydrogen-bond formation in the considered complexes

Complex	Nonconventional hydrogen bond	Δr(C1–H2) (mÅ)	$\Delta\nu$(C1–H2) (cm^{-1})
FN-1	C1–H2···N3	1.3	−15.5
FP-1	C1–H2···P3	0.2	−0.3
FAs-1	C1–H2···As3	0.4	−1.0
FSb-1	C1–H2···Sb3	0.6	−6.9
ClN-1	C1–H2···N3	5.4	−79.7
ClP-1	C1–H2···P3	1.6	−22.5
ClAs-1	C1–H2···As3	1.6	−22.5
ClSb-1	C1–H2···Sb3	1.9	−31.1
BrN-1	C5–H6···N3	7.0	−107.8
BrP-1	C1–H2···P3	2.2	−35.4
BrAs-1	C1–H2···As3	2.2	−35.0
BrSb-1	C1–H2···Sb3	2.5	−44.2
FN-2	C1–H2···N3	1.3	−15.9
FP-2	C1–H2···P3	0.2	0.2
FAs-2	C1–H2···As3	0.4	−1.1
FSb-2	C1–H2···Sb3	0.6	−6.8
ClN-2	C1–H2···N3	5.3	−79.6
ClP-2	C1–H2···P3	1.6	−22.4
ClAs-2	C1–H2···As3	1.6	−21.8
ClSb-2	C1–H2···Sb3	1.9	−30.7
BrN-2	C1–H2···N3	7.1	−110.1
BrP-2	C1–H2···P3	2.2	−34.8
BrAs-2	C1–H2···As3	2.1	−34.2
BrSb-2	C1–H2···Sb3	2.4	−43.4

stretching vibration is governed mainly by an electron density increase in the σ^*(C–H) orbital, which dominates over the small increase in the s-character of the C(H) orbital.

For complexes with the same proton donor CHX_3, the red shift of the C–H bond increases in the order C–H···As ≈ C–H···P < C–H···Sb < C–H···N. For example, in the **BrY-1** series, the $\Delta\nu_{(C-H)}$ value is −35.4 cm^{-1} for C–H···P, −35.0 cm^{-1} for C–H···As, −44.2 cm^{-1} for C–H···Sb, and −107.8 cm^{-1} for C–H···N (Table 3). On this basis, the red shift associated with the C–H···N interaction is twice larger than that of C–H···Sb and more than three times larger than those of C–H···P and C–H···As, confirming the substantially stronger nature of the C–H···N hydrogen bonds. We find that the red shifts of the C–H···N interactions obtained in the present work are larger than those reported at the MP2/6-311++G(d,p) level[36] and M06-2X/def2-TZVP.[49] Specifically, in those studies the $\Delta\nu_{(C-H)}$ value for CHF_3···NH_3 is only −2 to −3 cm^{-1}, whereas it reaches −15.5 cm^{-1} in the present work, with even larger discrepancies observed for $CHCl_3$···NH_3 and $CHBr_3$···NH_3. Nevertheless, the red shifts reported here remain significantly smaller than the values predicted at the B3LYP/6-311++G(d,p) level, which are up to ∼28 cm^{-1} larger in the case of $CHCl_3$···NH_3.[46] These comparisons indicate that the predicted vibrational frequency shifts in the considered complexes depend strongly on the computational method employed.

Interestingly, the red shift associated with the C–H···Sb interaction is stronger than those of C–H···P and C–H···As, despite the lower proton affinity of SbH_3 compared with PH_3 and AsH_3. This observation of red shift magnitude deviates from earlier expectations based on only proton affinity considerations.[36,75] However, in the Sb-containing complexes, the much higher polarizability of Y=Sb gives rise to $E_{inter}[n(Sb) \rightarrow \sigma^*(C1–H2)]$ values that, although significantly smaller than those for Y=N, are comparable to or larger than the corresponding values for Y=P and As (Table 2). Together with the relatively smaller changes of intramolecular hyperconjugation energies (ΔE_{intra}) in the Sb complexes compared with the P- and As-containing systems, this leads to a significantly increased population of the σ^*(C–H) antibonding orbital in the Sb-containing complexes (Table 2). For example, $\Delta\sigma^*$(C1–H2) is 8.9 me for **ClSb-1**, whereas it is only 6.5 me for **ClAs-1** and 4.7 me for **ClP-1**. As a result, the C–H bond is more strongly weakened, leading to a larger C–H vibrational red shift in the C–H···Sb hydrogen bonds than in the corresponding C–H···P and C–H···As ones. Therefore, the observed red-shift trend in the C–H···P/As/Sb hydrogen bonds is governed primarily by atomic polarizability of proton acceptor and the increased population of the σ^*(C–H) antibonding orbital rather than by proton affinity.

For the complexes with the same proton acceptor YH_3, the magnitude of the C–H red shift increases systematically as X in the proton donor CHX_3 changes from F to Cl to Br. For example, as shown in Table 3, in the **XN-1** series, the $\Delta\nu_{(C-H)}$ values are from −15.5 cm^{-1} (**FN-1**) to −79.7 cm^{-1} (**ClN-1**) and further to −107.8 cm^{-1} (**BrN-1**), showing that the C–H red shift in $CHBr_3$ is approximately seven times larger than that in CHF_3 and about 1.5 times larger than that in $CHCl_3$. A similar tendency is observed for Y=P, As, and Sb. These trends are consistent with previous investigations and can be attributed to the enhanced polarity of the C–H bond as X becomes heavier (F < Cl < Br).[36,46] For the NH_3-containing complexes, the increase in the C–H red shift from X = F to Cl to Br can be rationalized by the strengthening coulombic interaction between the positively polarized hydrogen atom and the negatively charged nitrogen atom. One can see from Table 2 that the NBO q(H2) charge increases significantly from **FN-1/2** to **ClN-1/2** and **BrN1/2**, whereas q(N3) remains nearly constant and strongly negative, leading to enhanced electrostatic attraction in the C–H···N hydrogen bond. This stronger Coulomb interaction, in turn, weakens the C–H bond and produces a larger C–H red shift. Unlike the NH_3-containing complexes, the corresponding trends in the C–H···P/As/Sb hydrogen bonds as X changes from F to Br can not be explained by electrostatics alone, as the acceptor atoms Y do not carry significant negative charge (Table 2). In these cases, the interaction is explained mainly by the higher polarizability of the proton acceptor atom, which facilitates n(Y3) → σ^*(C1–H2) charge transfer, thereby increasing the population of the σ^*(C1–H2) antibonding orbital and producing larger vibrational red shifts.

3.3. Interaction energies of complexes and the SAPT2+ analysis

The interaction energies of the obtained complexes, listed in Table 4, are all negative, ranging from −3.0 to −18.3 kJ mol^{-1} with both ZPE and BSSE corrections. This indicates that all complexes are stable on the potential energy surface. For each

Table 4 Interaction energies corrected for both ZPE and BSSE (ΔE^*, in kJ mol^{-1}) for the studied complexes

Complex	ΔE^* (kJ mol^{-1})	Complex	ΔE^* (kJ mol^{-1})
FN-1	−14.1	**FN-2**	−14.1
FP-1	−5.5	**FP-2**	−5.6
FAs-1	−4.4	**FAs-2**	−4.4
FSb-1	−3.0	**FSb-2**	−3.0
ClN-1	−17.3	**ClN-2**	−17.3
ClP-1	−8.1	**ClP-2**	−8.1
ClAs-1	−7.2	**ClAs-2**	−7.1
ClSb-1	−5.6	**ClSb-2**	−5.5
BrN-1	−17.8	**BrN-2**	−18.3
BrP-1	−8.8	**BrP-2**	−8.8
BrAs-1	−8.0	**BrAs-2**	−7.8
BrSb-1	−6.2	**BrSb-2**	−6.2

$CHX_3\cdots YH_3$ pair, the eclipsed and staggered conformations exhibit very similar interaction strengths, with energy differences typically below 0.4 kJ mol^{-1}. This negligible difference is consistent with the nearly identical strengths of the C–H···Y hydrogen bonds in the two conformations, as mentioned in the AIM analysis. It is noted that the largest difference is observed for the Br-containing complexes, which should be attributed to the larger size and higher polarizability of Br, leading to enhanced sensitivity of short-range exchange and polarization contributions to noticeable difference of two configurations.

For the same X of CHX_3 proton donor, the interaction energies systematically become less negative as Y in YH_3 varies in the order N < P < As < Sb. Namely, the ΔE^* values fall within the ranges −14.1 to −18.3 kJ mol^{-1} for Y═N, −5.5 to −8.8 kJ mol^{-1} for Y═P, −4.4 to −8.0 kJ mol^{-1} for Y═As, and −3.0 to −6.2 kJ mol^{-1} for Y═Sb. Accordingly, the N-containing complexes are more than twice as stable as their P-, As-, and Sb-containing counterparts. When Y in YH_3 is fixed, the interaction energies become progressively more negative as the proton donor changes from CHF_3 to $CHCl_3$ to $CHBr_3$. Indeed, the ΔE^* ranges of −14.1 to −3.0 kJ mol^{-1} for $CHF_3\cdots YH_3$, −17.3 to −5.5 kJ mol^{-1} for $CHCl_3\cdots YH_3$, and −18.3 to −6.2 kJ mol^{-1} for $CHBr_3\cdots YH_3$ indicate that the Br-containing species are approximately 1.3–2.0 times more stable than their F-containing counterparts. These monotonic increases in stability are fully consistent with the AIM analysis, which shows that the strength of the C–H···Y hydrogen bond follows the same order. We note that the interaction energies of $CHX_3\cdots NH_3$ complexes obtained in this work at the CCSD(T)/aug-cc-pVTZ level are consistently more negative than those reported using the smaller 6-311++G(3df,2pd) and 6-311++G(d,p) basis sets in earlier studies.[36,50] For instance, for the $CHCl_3\cdots NH_3$ complex, the reported interaction energies were −15.4 kJ mol^{-1} at the CCSD(T)/6-311++G(3df,2pd) level and −15.1 kJ mol^{-1} at the CCSD(T)/6-311++G(d,p) level, both less negative than the values (around −17 kJ mol^{-1}) obtained in this work.

We now evaluate the contributions of the individual energy components obtained from SAPT2+ to the overall stability of the complexes. As the energy contributions for each complex are nearly identical for the two conformations, with only the energy

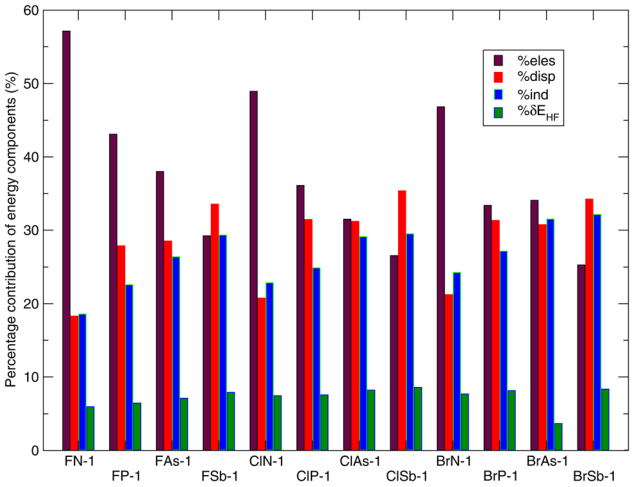

Fig. 2 The percentage contribution of energetic components obtained from SAPT2+ to the stability of XY-1 complexes.

decomposition of the **XY-1** complex is shown in Fig. 2, while the detailed results for all complexes are summarized in Table S1 of SI. It can be seen from Fig. 2 that the attractive component of the $CHX_3\cdots YH_3$ interaction is mainly governed by electrostatic (%elst), dispersion (%disp), and induction (%ind) contributions, with their relative importance depending on the specific complex. For the strongest complexes, **XN**, the electrostatic term is clearly dominant. For example, in these complexes, the electrostatic contribution reaches about 45%, which is about two to three times larger than the induction and dispersion contributions, each accounting for roughly 18–25%. This distribution of energy components demonstrates that the C–H···N hydrogen bonds are mainly electrostatic in nature, while induction and dispersion offer supportive stabilization. As Y becomes heavier (N → P → As → Sb), the importance of the electrostatic contribution decrease, while both induction and dispersion contributions become increasingly competitive. Indeed, in the P- and As-containing complexes, the electrostatic contribution decreases to approximately 31–43%, while the dispersion fraction increases to about 28–35% and the induction contribution rises to roughly 23–32%. Consequently, for Y═P/As/Sb, the hydrogen bond is no longer purely electrostatically dominated but instead reflects a more balanced interplay of electrostatics, polarization, and dispersion. Notably, in the Sb-containing complexes, both dispersion and induction contributions, in the range of approximately 29–35%, exceed the electrostatic term, which accounts for about 25–29%. This behavior occurs because the C–H···Y hydrogen bond becomes weaker and less directional as Y becomes heavier, reducing electrostatic interactions and increasing the relative importance of polarization and dispersion.

For a given proton acceptor YH_3, the relative electrostatic contribution generally decreases, while dispersion and induction become increasingly important as X changes from F to Cl to Br in CH_3X (see Fig. 2). Moreover, the change is more pronounced from F to Cl than from Cl to Br. For example, in the N-containing complexes, the electrostatic contribution decreases by about 8% when going from $CH_3F\cdots NH_3$ (57.1%) to

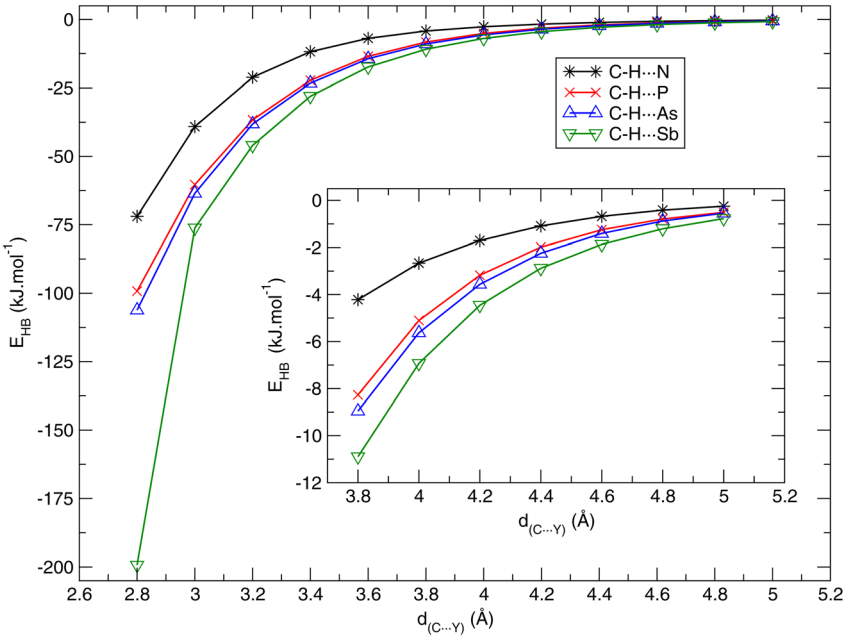

Fig. 3 Changes in strength of the individual hydrogen bonds in the $CHCl_3\cdots YH_3$ (Y=N, P, As, Sb) complexes as a function of the C···Y separation.

$CH_3Cl\cdots NH_3$ (48.9%), but by only about 2% when going from $CH_3Cl\cdots NH_3$ to $CH_3Br\cdots NH_3$.

3.4. Distance-dependent characteristics of hydrogen bonds in studied systems

To gain deeper insight into the origin of the vibrational shifts observed for C–H···Y (Y=N, P, As, Sb) hydrogen bonds, it is useful to move beyond equilibrium structures and examine how their characteristics evolve as a function of intermolecular distance along the potential energy surface. To this end, the $CHCl_3\cdots YH_3$ complexes in the staggered conformation are selected as representative systems, and the C···Y distance in these complexes is systematically varied from 2.8 to 5.0 Å in increments of 0.2 Å.

We first examine the strength of the individual hydrogen bonds presented in Fig. 3 and summarized in Table S2. As shown in Fig. 3, the strength of the C–H···Y hydrogen bonds in the $CHCl_3\cdots YH_3$ complexes decreases rapidly with increasing C···Y separation for all proton acceptors considered. At short C···Y distances, the hydrogen-bond strength follows the decreasing order C–H···Sb > C–H···As > C–H···P > C–H···N, which correlates with the lowering polarizability of the proton acceptor atom. Notably, the C–H···Sb interaction exhibits a markedly larger distance dependence in the very short-range region (2.8–3.0 Å) than the corresponding C–H···N/P/As interactions. This behavior arises from the higher polarizability of Sb as compared to the N/P/As atom, which amplifies short-range induction and dispersion contributions, and the rapid decay of these components with increasing separation leads to the pronounced change in hydrogen-bond strength observed. Although the interaction weakens significantly upon elongation of the C···Y distance, the same ordering is preserved over the entire range examined, indicating that acceptor polarizability plays a key role in governing the hydrogen-bond strength as the C···Y separation changes. We note that the E_{HB} values evaluated at C···Y distances corresponding to the equilibrium geometries are in good agreement with the hydrogen-bond energies obtained for the optimized structures (Table 1 and S2).

We now move to discuss the variation of the C–H stretching frequency associated with the C–H···Y hydrogen bonds, together with the corresponding SAPT2+ energy components as the C···Y separation changes from 2.8–5.0 Å. The resulting trends are illustrated in Fig. 4 and 5 and summarized in Tables S3 and S4 of SI. Fig. 4 shows that the change in the C–H stretching frequency strongly depends on both the C···Y distance and the identity of Y. At short separations ($d_{C\cdots Y}$ = 2.8–3.4 Å), the C–H···N hydrogen bond exhibits a red shift throughout this region, with $\Delta\nu_{(C-H)}$ decreasing from −111.4 cm^{-1} at 2.8 Å to −66.4 cm^{-1} at 3.4 Å. In contrast, the C–H···P/As/Sb interactions exhibit pronounced blue-shifting behavior, with $\Delta\nu$ values of 295.2, 410.3, and 734.9 cm^{-1} for P, As, and Sb at a C···Y distance of 2.8 Å, and these values decrease rapidly as the separation increases, approaching near-zero shifts of 0.3, 11.2, and 44.7 cm^{-1} at $d_{C\cdots Y}$ = 3.4 Å. Moreover, the magnitude of the blue shift increases systematically from P to As to Sb, indicating a stronger short-range perturbation of the C–H bond for the heavier pnictogens. In the intermediate distances ($d_{C\cdots Y}$ = 3.6–4.2 Å), the C–H···N hydrogen bond remains red-shifting. However, for the P-, As-, and Sb-containing complexes, the blue-shifted behavior observed at shorter separations is inverted to a red shift at a C···Y distance of 3.6 Å. At equilibrium distances ($d_{C\cdots Y}$ = 3.8–4.0 Å), the red shift is stronger for the C–H···Sb interaction than for C–H···P/As, which is consistent with the observation discussed in Section 3.2. At very large distances ($d_{C\cdots Y}$ = 4.2–5.0 Å), the magnitude of the red shift observed in all the hydrogen bonds decreases rapidly. Interestingly, beyond 4.4 Å, the magnitude of

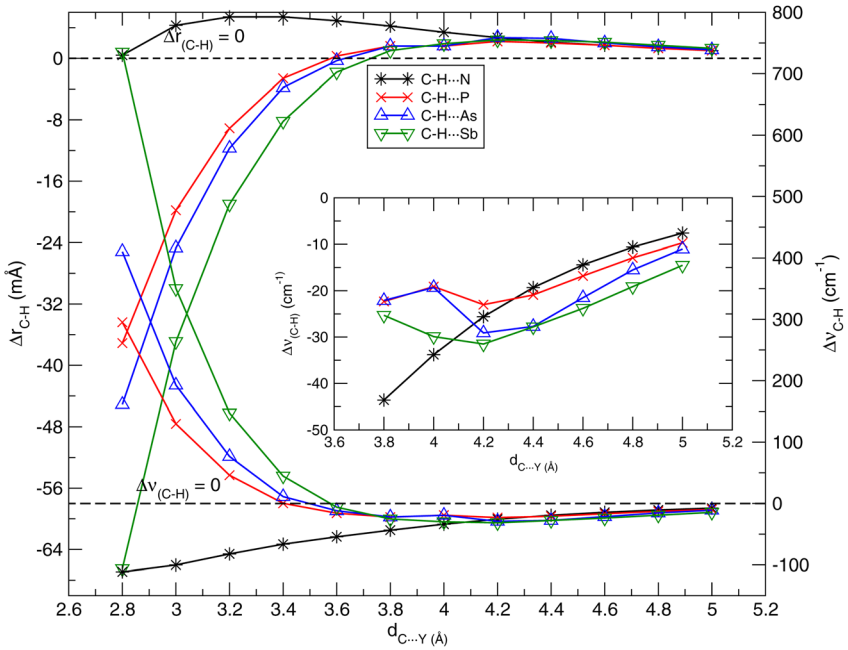

Fig. 4 Changes in the C–H bond length (Δr, mÅ) and stretching frequency (Δν, cm^{-1}) in the $CHCl_3\cdots YH_3$ (Y═N, P, As, and Sb) complexes as a function of the C···Y separation.

the red shift of the C–H stretching frequency decreases systematically as Y changes from Sb to As to P to N. This inversion of the trend can be attributed to a change in the dominant interaction character: whereas the C–H···N hydrogen bond is strongest at short and intermediate distances due to its highly directional electrostatic nature, at larger separations the residual perturbation is governed primarily by the polarizability of Y, resulting in larger red shifts of the C–H stretching vibration for the heavier pnictogens.

The absolute magnitudes of all attractive terms calculated by SAPT2+ decrease monotonically with increasing C···Y distance (see Table S4). However, their relative percentage contributions change significantly because these components decay at different rates. At short intermolecular separations, induction

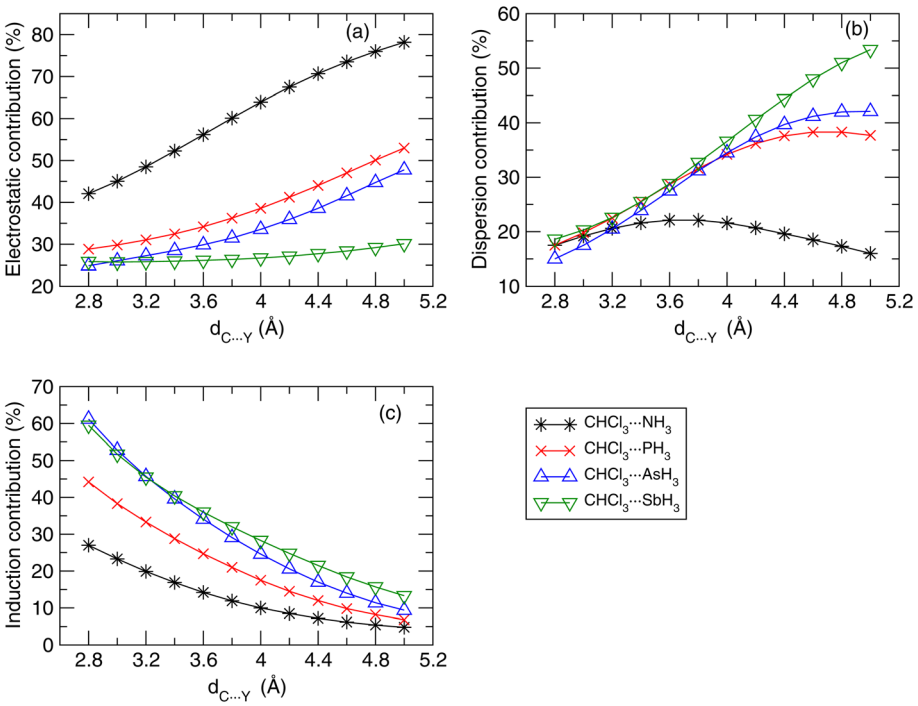

Fig. 5 The percentage contribution of electrostatic (a), dispersion (b), and induction (c) components obtained from SAPT2+ to the stability of $CHCl_3\cdots YH_3$ complexes as a function of the C···Y separation.

plays a dominant role in stabilizing the interaction, particularly for the heavier pnictogens; however, its importance decreases rapidly as the C⋯Y distance increases (see Fig. 5c). For instance, for Y=As and Sb, induction contributes about 60% of the total attractive interaction at a C⋯Y distance of 2.8 Å, but decreases sharply with increasing separation, falling below 30% at around 3.8–4.0 Å and to less than 15% in the long-range regime. This behavior indicates that polarization effects are intrinsically short-to intermediate-range in nature, even for highly polarizable pnictogens.

In contrast to induction, the relative electrostatic contribution increases systematically with increasing C⋯Y distance for all complexes (see Fig. 5a). For Y=N, electrostatics dominates over the entire distance range, with %elst increasing from about 42% at 2.8 Å to nearly 80% at large separations. For Y=P and As, %elst rises steadily from approximately 25–30% at short distances to about 50% in the long-range regime. However, for Y=Sb, the electrostatic contribution increases more modestly, from about 26% to roughly 30% at large distances. The dispersion contribution exhibits a distance dependence that differs from that of electrostatics (see Fig. 5b). For Y=N, the dispersion fraction increases slightly from about 18% at 2.8 Å to a maximum of approximately 22% at intermediate separations, and then gradually decreases to about 16% at 5.0 Å. However, for the heavier pnictogens (Y=P, As, and Sb), %disp is relatively small at short distances because the interaction is dominated by induction. As the C⋯Y distance increases and the induction contribution decays rapidly, the relative importance of dispersion increases, reaching maxima of roughly 38% for Y=P, 42% for Y=As, and over 50% for Y=Sb at large separations.

Taken together, the distance-dependent SAPT2+ analysis provides a clear physical interpretation of the C–H stretching frequency shifts associated with the C–H⋯Y hydrogen bonds discussed above. The C–H⋯N hydrogen bonds are dominated by electrostatic interactions over the entire distance range considered. In contrast, the C–H⋯P/As/Sb interactions are governed primarily by induction effects at short separations, which strengthen the C–H bond and give rise to blue-shifting behavior. As the C⋯Y distance increases, the induction contribution decays rapidly, leading to a crossover toward interactions increasingly governed by electrostatics and dispersion. This redistribution of interaction components correlates directly with the transition from blue-to red-shifting behavior observed for the C–H⋯P/As/Sb hydrogen bonds, with dispersion becoming increasingly important in the long-range regime.

4. Conclusive remarks

In this work, we present a comprehensive comparative study of nonconventional C–H⋯Y hydrogen bonds (Y=N, P, As, Sb) in complexes formed between haloforms (CHX_3, X = F, Cl, Br) and pnictogen trihydrides (YH_3), with particular emphasis on interactions involving the heavier pnictogen elements. On the basis of these results, the main findings are summarized below. The C–H⋯Y hydrogen-bond strength in the considered complexes increases across the pnictogen series in the order Sb < As ≈ P < N, with C–H⋯N interactions being about two to three times stronger than the corresponding C–H⋯P/As/Sb ones. The hydrogen bonds are predominantly red-shifting, with the magnitude of the shift increasing in the order C–H⋯As ≈ C–H⋯P < C–H⋯Sb < C–H⋯N. The unusually large red shifts observed for the C–H⋯Sb interactions relative to C–H⋯P/As arise from the high polarizability of Sb and the associated increase in σ^*(C–H) antibonding orbital population, rather than from proton affinity. In contrast, for C–H⋯N hydrogen bonds, the increase in the red shift from X = F to Cl to Br is driven primarily by stronger coulombic attraction between the polarized hydrogen atom and the negatively charged nitrogen atom.

The eclipsed and staggered conformations of each CHX_3⋯YH_3 complex show very similar interaction energies. When the CHX_3 proton donor is fixed, the interaction energy increases in magnitude as the proton acceptor atom Y in YH_3 changes in the order N < P < As < Sb. For a fixed YH_3 acceptor, the interaction energy becomes more negative as the proton donor changes from CHF_3 to $CHCl_3$ to $CHBr_3$. SAPT2+ analysis reveals that the nature of C–H⋯Y hydrogen bonds in the complexes strongly depends on the identity of the YH_3 acceptor. Specifically, the C–H⋯N interactions are dominated by electrostatic effects, while in the C–H⋯P/As/Sb interactions the electrostatic contribution diminishes, with induction and dispersion becoming increasingly important, leading to a more balanced distribution of attractive interactions.

Examination of the C–H stretching frequency shifts as a function of the C⋯Y separation shows that the C–H⋯P/As/Sb hydrogen bonds undergo a clear transition from blue-shifting to red-shifting behavior at a C⋯Y distance of about 3.6 Å, whereas the C–H⋯N interaction remains red-shifting over the entire distance range, reflecting its consistently stronger hydrogen-bond character. Distance-dependent SAPT2+ analysis further indicates that the C–H⋯N hydrogen bonds are dominated by electrostatic interactions throughout the entire distance range. In contrast, the blue-shifting behavior of the C–H⋯P/As/Sb hydrogen bonds at short separations is governed primarily by induction effects, whereas at larger C⋯Y distances the diminishing induction contribution together with the increasing role of dispersion leads to red-shifting behavior.

These obtained results provide a physical framework for understanding nonconventional C–H⋯Y hydrogen bonding across the pnictogen series and highlight the critical role of acceptor polarizability in governing the interaction energies of complexes and the changes of C–H vibrational frequency shifts.

Conflicts of interest

There are no conflicts to declare.

Data availability

The authors confirm that the data supporting the findings of this study are available within the article and its supplementary information (SI). Supplementary information is available. See DOI: https://doi.org/10.1039/d6ra00247a.

Acknowledgements

This research was funded by the Vietnam National Foundation for Science and Technology Development (NAFOSTED) under grant number 104.06-2023.49.

References

1 G. A. Jeffrey and W. Saenger, *Hydrogen Bonding in Biological Structures*, Springer, Berlin, 1991.
2 S. Scheiner, *Hydrogen Bonding: A Theoretical Perspective*, Oxford University Press, Oxford, 1997.
3 C. N. Pace, H. Fu, K. L. Fryar, J. Landua, S. R. Trevino, D. Schell, R. L. Thurlkill, S. Imura, J. M. Scholtz, K. Gajiwala, J. Sevcik, L. Urbanikova, J. K. Myers, K. Takano, E. J. Hebert, B. A. Shirley and G. R. Grimsley, *Protein Sci.*, 2014, **23**, 652–666.
4 Y. Takano, H. X. Kondo and H. Nakamura, *Biophys. Rev.*, 2023, **14**, 1369–1378.
5 Y. P. Yurenko, R. O. Zhurakivsky, S. P. Samijlenko and D. M. Hovorun, *J. Biomol. Struct. Dyn.*, 2011, **29**, 51–65.
6 G. Ghosal and K. Muniyappa, *Biochem. Biophys. Res. Commun.*, 2006, **343**, 1–7.
7 Y. Qi, D. Zhou, J. L. Kessler, R. Qiu, S. M. Yu, G. Li, Z. Qin and Y. Li, *Chem. Sci.*, 2022, **13**, 12567–12576.
8 J. Chen, Z. Wang, Z. Deng, L. Chen, X. Wu, Y. Gao, Y. Hu, M. Li and H. Wang, *Front. Chem.*, 2023, **11**, 1200644.
9 H. Yue, Y. Wang, S. Luo, J. Guo, J. Jin, G. Li, Z. Meng, L. Zhang, D. Zhou, Y. Zhen and W. Hu, *Sci. Adv.*, 2024, **10**, eadq0171.
10 M. Irimia-Vladu, Y. Kanbur, F. Camaioni, M. E. Coppola, C. Yumusak, C. V. Irimia, A. Vlad, A. Operamolla, G. M. Farinola, G. P. Suranna, N. Gonzalez-Benitez, M. C. Molina, L. F. Bautista, H. Langhals, B. Stadlober, E. D. Glowacki and S. N. Sariciftci, *Chem. Mater.*, 2019, **31**, 6315–6346.
11 S. J. D. Lugger, S. J. A. Houben, Y. Foelen, M. G. Debije, A. P. H. J. Schenning and D. J. Mulder, *Chem. Rev.*, 2021, **122**, 4946–4975.
12 Z. Wang, M. Si, J. Han, Y. Shen, G. Yin, K. Yin, P. Xiao and T. Chen, *Angew. Chem., Int. Ed.*, 2025, **64**, e202416095.
13 P. Song and H. Wang, *Adv. Mater.*, 2020, **32**, 1901244.
14 A.-E. Segneanu, L. E. Bejenaru, C. Bejenaru, A. Blendea, G. D. Mogoşanu, A. Bita and E. R. Boia, *Polymers*, 2025, **17**, 2026.
15 Z. Ling, J. V. Edwards, S. Nam, F. Xu and A. D. French, *Cellulose*, 2020, **27**, 1207–1224.
16 T. Zhang, Y. Hu, Y. Dong, S. Jiang and X. Han, *Polymers*, 2025, **17**, 2064.
17 Y. Wang, H. He, C. Wang, Y. Lu, K. Dong, F. Huo and S. Zhang, *JACS Au*, 2022, **2**, 543–561.
18 P. Zhang, X. Ma, Z. Tu, X. Zhang, X. Hu and Y. Wu, *Green Energy Environ.*, 2025, **10**, 560–572.
19 G. R. Desiraju and T. Steiner, *The Weak Hydrogen Bond: in Structural Chemistry and Biology*, Oxford University Press, Oxford (USA), 2001.
20 G. A. Jeffrey, *An Introduction to Hydrogen Bonding*, Oxford University Press, Oxford (USA), 1997.
21 E. D. Isaacs, A. Shukla, P. M. Platzman, D. R. Hamann, B. Barbiellini and C. A. Tulk, *Phys. Rev. Lett.*, 1999, **82**, 600–603.
22 K. G. Tapan, N. S. Viktor, R. K. Patrick and R. D. Ernest, *J. Am. Chem. Soc.*, 2000, **122**, 1210–1214.
23 S. J. Grabowski, *Chem. Rev.*, 2011, **111**, 2597–2625.
24 M. S. Gordon and J. H. Jensen, *Acc. Chem. Res.*, 1996, **29**, 536–543.
25 I. V. Alabugin, M. Manoharan, S. Peabody and F. Weinhold, *J. Am. Chem. Soc.*, 2003, **125**, 5973–5987.
26 J. Joseph and E. D. Jemmis, *J. Am. Chem. Soc.*, 2007, **129**, 4620–4632.
27 P. Hobza and Z. Havlas, *Chem. Rev.*, 2000, **100**, 4253–4264.
28 X. Li, L. Liu and H. B. Schlegel, *J. Am. Chem. Soc.*, 2002, **124**, 9639–9647.
29 Y. Mo, C. Wang, L. Guan, B. Braïda, P. C. Hiberty and W. Wu, *Chem. – Eur. J.*, 2014, **20**, 8444–8452.
30 X. Chang, Y. Zhang, X. Weng, P. Su, W. Wu and Y. Mo, *J. Phys. Chem. A*, 2016, **120**, 2749–2756.
31 C. Wang, D. Danovich, S. Shaik and Y. Mo, *J. Chem. Theory Comput.*, 2017, **13**, 1626–1637.
32 L. Pejov and K. Hermansson, *J. Chem. Phys.*, 2003, **119**, 313–324.
33 P. Hobza and Z. Havlas, *Chem. Phys. Lett.*, 1999, **303**, 447–452.
34 J. S. Murray, M. C. Concha, P. Lane, P. Hobza and P. Politzer, *J. Mol. Model.*, 2008, **14**, 699–704.
35 Y. Mao and M. Head-Gordon, *J. Phys. Chem. Lett.*, 2019, **10**, 3899–3905.
36 N. T. H. Man, P. L. Nhan, V. Vo, D. T. Quang and N. T. Trung, *Int. J. Quantum Chem.*, 2017, **117**, e25338.
37 N. T. T. Cuc, C.-T. D. Phan, V. Vien, T. Q. Duong and N. T. Trung, *J. Phys. Chem. A*, 2021, **125**, 10291–10302.
38 N. T. Trung, N. T. T. Trang, V. T. Ngan, D. T. Quang and M. T. Nguyen, *RSC Adv.*, 2016, **6**, 31401–31409.
39 N. N. Tri, N. T. H. Man, N. L. Tuan, N. T. T. T. Trang, D. T. Q. Quang and N. T. Trung, *Theor. Chem. Acc.*, 2017, **136**, 10.
40 T.-N. Huynh, N. T. M. Nguyet, B. D. Ai and N. T. Trung, *Phys. Chem. Chem. Phys.*, 2025, **27**, 14966–14975.
41 N. T. Trung, T. T. H. Hue and M. T. Nguyen, *Phys. Chem. Chem. Phys.*, 2009, **11**, 926–933.
42 J.-M. Fan, L. Liu and Q.-X. Guo, *Chem. Phys. Lett.*, 2002, **365**, 464–472.
43 W. A. Herrebout, S. M. Melikova, S. N. Delanoye, K. S. Rutkowski, D. N. Shchepkin and B. J. van der Veken, *J. Phys. Chem. A*, 2005, **109**, 3038–3044.
44 F. Ito, *J. Chem. Phys.*, 2012, **137**, 014505.
45 B. Behera and P. K. Das, *J. Phys. Chem. A*, 2019, **123**, 1830–1839.
46 G. Baburao, A. Esakkimuthu and G. Ragupathy, *Comput. Theor. Chem.*, 2024, **1242**, 114935.
47 K. S. Rutkowski, A. Karpfen, S. M. Melikova, W. A. Herrebout, A. Koll, P. Wolschann and B. J. van der Veken, *Phys. Chem. Chem. Phys.*, 2009, **11**, 1551–1563.

48 L. Zhang, L. Pei, D. Li and H. Bian, *J. Phys. Chem. A*, 2024, **128**, 6898–6907.
49 S. Scheiner, *Phys. Chem. Chem. Phys.*, 2025, **27**, 6800–6809.
50 M. Hippler, *J. Chem. Phys.*, 2007, **127**, 084312.
51 F. H. Westheimer, *Science*, 1987, **235**, 1173–1178.
52 R. J. Bowell, C. N. Alpers, H. E. Jamieson, D. K. Nordstrom and J. Majzlan, *Rev. Mineral. Geochem.*, 2014, **79**, 1–16.
53 L. da Costa, J. Zopfi, C. Alewell, M. F. Lehmann and M. Lenz, *Environ. Sci.: Processes Impacts*, 2025, **27**, 833–848.
54 A. S. Hansen, L. Du and H. G. Kjaergaard, *J. Phys. Chem. Lett.*, 2014, **5**, 4225–4231.
55 K. Lisac, F. Topić, M. Arhangelskis, S. Cepić, P. A. Julien, C. W. Nickels, A. J. Morris, T. Friščić and D. Cinčić, *Nat. Commun.*, 2019, **10**, 61.
56 M. J. Frisch, G. W. Trucks, H. B. Schlegel, G. E. Scuseria, M. A. Robb, J. R. Cheeseman, G. Scalmani, V. Barone, G. A. Petersson, H. Nakatsuji, X. Li, M. Caricato, A. V. Marenich, J. Bloino, B. G. Janesko, R. Gomperts, B. Mennucci, H. P. Hratchian, J. V. Ortiz, A. F. Izmaylov, J. L. Sonnenberg, D. Williams-Young, F. Ding, F. Lipparini, F. Egidi, J. Goings, B. Peng, A. Petrone, T. Henderson, D. Ranasinghe, V. G. Zakrzewski, J. Gao, N. Rega, G. Zheng, W. Liang, M. Hada, M. Ehara, K. Toyota, R. Fukuda, J. Hasegawa, M. Ishida, T. Nakajima, Y. Honda, O. Kitao, H. Nakai, T. Vreven, K. Throssell, J. A. Montgomery Jr, J. E. Peralta, F. Ogliaro, M. J. Bearpark, J. J. Heyd, E. N. Brothers, K. N. Kudin, V. N. Staroverov, T. A. Keith, R. Kobayashi, J. Normand, K. Raghavachari, A. P. Rendell, J. C. Burant, S. S. Iyengar, J. Tomasi, M. Cossi, J. M. Millam, M. Klene, C. Adamo, R. Cammi, J. W. Ochterski, R. L. Martin, K. Morokuma, O. Farkas, J. B. Foresman and D. J. Fox, *Gaussian 16, Revision A.03*, Gaussian Inc., Wallingford CT, 2016.
57 S. F. Boys and F. J. M. P. Bernardi, *Mol. Phys.*, 1970, **19**, 553–566.
58 T. A. Keith, *AIMAll, Version 19.10.12*, TK Gristmill Software, Overland Park, KS, 2019.
59 R. F. W. Bader, *Acc. Chem. Res.*, 1985, **18**, 9–15.
60 R. F. W. Bader, *Chem. Rev.*, 1991, **91**, 893–928.
61 M. Ziółkowski, S. J. Grabowski and J. Leszczynski, *J. Phys. Chem. A*, 2006, **110**, 6514–6521.
62 E. Espinosa, E. Molins and C. Lecomte, *Chem. Phys. Lett.*, 1998, **285**, 170–173.
63 J. Contreras-García, E. R. Johnson, S. Keinan, R. Chaudret, J.-P. Piquemal, D. N. Beratan and W. Yang, *J. Chem. Theory Comput.*, 2011, **7**, 625–632.
64 E. R. Johnson, S. Keinan, P. Mori-Sánchez, J. Contreras-García, A. J. Cohen and W. Yang, *J. Am. Chem. Soc.*, 2010, **132**, 6498–6506.
65 E. D. Glendening, C. R. Landis and F. Weinhold, *J. Comput. Chem.*, 2019, **40**, 2234–2241.
66 J. M. Turney, A. C. Simmonett, R. M. Parrish, E. G. Hohenstein, F. A. Evangelista, J. T. Fermann, B. J. Mintz, L. A. Burns, J. J. Wilke, M. L. Abramavicius, N. J. Russell, C. L. Schafer, G. G. Su, H. F. Bozkaya, A. Y. Sokolov, R. D. Remigio, P. M. Richard, K. H. Yang, T. R. Crawl, M. R. Reed, B. P. Pritchard, T. D. Crawford, J. S. Sherrill, R. A. King, E. F. Valeev, H. F. Schaefer III, K. K. Baldridge, J. B. Foresman and C. D. Sherrill, *Wiley Interdiscip. Rev.: Comput. Mol. Sci.*, 2012, **2**, 556–565.
67 U. Koch and P. L. A. Popelier, *J. Phys. Chem.*, 1995, **99**, 9747–9754.
68 C.-T. D. Phan, N. T. A. Nhung and N. T. Trung, *ACS Omega*, 2020, **5**, 14408–14416.
69 N. T. T. Cuc, C.-T. D. Phan, N. T. A. Nhung, M. T. Nguyen, N. T. Trung and V. T. Ngan, *J. Phys. Chem. A*, 2021, **125**, 10291–10302.
70 L. T. T. Quyen, B. N. Tung, P. N. Thach, N. N. Tri and N. T. Trung, *RSC Adv.*, 2024, **14**, 14114–14125.
71 N. T. An, V. T. Ngan and N. T. Trung, *Phys. Chem. Chem. Phys.*, 2024, **26**, 22775–22789.
72 E. P. L. Hunter and S. G. Lias, *J. Phys. Chem. Ref. Data*, 1998, **27**, 413–656.
73 M. Born, S. Ingemann and N. M. M. Nibbering, *Int. J. Mass Spectrom.*, 2000, **194**, 103–113.
74 P. Schwerdtfeger and J. K. Nagle, *Mol. Phys.*, 2019, **117**, 1200–1225.
75 H. Q. Dai, N. N. Tri, N. T. Thu Trang and N. T. Trung, *RSC Adv.*, 2014, **4**, 13901–13908.